CDDpress

www.nature.com/cdd

ARTICLE

Check for updates

HSC70 mediated autophagic degradation of oxidized PRL2 is responsible for osteoclastogenesis and inflammatory bone destruction

Qi Li[1,7], Tao Yue[2,7], Xinyue Du[1], Zaiming Tang[3], Jinjie Cui[4], Weifeng Wang[2], Wenjie Xia[2], Baiyang Ren[1], Shuo Kan[1], Chang Li[1], Chenyun Wu[1], Xiaoyin Niu[1], Bin Li[1], Kaili Lin[4], Jian Luo[5], Guangjie Chen[1]✉ and Zhaojun Wang[1,6]✉

Inflammation leads to systemic osteoporosis or local bone destruction, however, the underlying molecular mechanisms are still poorly understood. In this study, we report that PRL2 is a negative regulator of osteoclastogenesis and bone absorption. Mice with PRL2 deficiency exhibit a decrease in bone volume and an increase in osteoclast numbers. PRL2 negatively regulates RANKL-induced reactive oxygen species production through the activation of RAC1, thus PRL2 deficient osteoclast precursors have both increased osteoclast differentiation ability and bone resorptive capacity. During inflammation, oxidized PRL2 is a selected substrate of HSC70 and conditions of oxidative stress trigger rapid degradation of PRL2 by HSC70 mediated endosomal microautophagy and chaperone-mediated autophagy. Ablation of PRL2 in mouse models of inflammatory bone disease leads to an increase in the number of osteoclasts and exacerbation of bone damage. Moreover, reduced PRL2 protein levels in peripheral myeloid cells are highly correlated with bone destruction in a mouse arthritis model and in human rheumatoid arthritis, while the autophagy inhibitor hydroxychloroquine blocked inflammation-induced PRL2 degradation and bone destruction in vivo. Therefore, our findings identify PRL2 as a new regulator in osteoimmunity, providing a link between inflammation and osteoporosis. As such, PRL2 is a potential therapeutic target for inflammatory bone disease and inhibition of HSC70 mediated autophagic degradation of PRL2 may offer new therapeutic tools for the treatment of inflammatory bone disease.

Cell Death & Differentiation (2023) 30:647–659; https://doi.org/10.1038/s41418-022-01068-y

INTRODUCTION

Inflammation in rheumatoid arthritis (RA), ankylosing spondylitis (AS), osteomyelitis and periodontitis leads to local bone destruction or systemic osteoporosis [1–3]. Although medical achievements have improved the treatment of these diseases, irreversible bone erosion is still a key outcome and correlates with functional deterioration [3, 4]. Thus, further detailed studies of cells and signals in this inflammatory process will provide a better understanding on inflammatory bone disease progression and reveal new potential therapeutic targets.

Osteoclasts are the principal effectors of inflammatory bone disease. They are large, multinucleated bone resorbing cells, which differentiate from the monocyte/macrophage lineage cells upon stimulation with macrophage colony-stimulating factor (M-CSF) and receptor activator of nuclear factor-κB ligand (RANKL) [5]. RANKL transduces its signal through the signaling receptor RANK and activation of RANK on mononuclear osteoclast precursors initiates various downstream pathways, including mitogen-activated protein kinase (MAPK) and nuclear factor-kappa-B (NF-κB) [6], while nuclear factor of activated T-cells cytoplasmic 1 (NFATc1) has been shown to be the master regulator of RANKL-induced osteoclast differentiation [7–9]. In addition, the redox balance exerts a vital role in regulating osteoclastogenesis. RANKL induces a transient and fast increase in reactive oxygen species (ROS) through the action of TRAF6, NOX1, and RAC1 [10, 11], leading to mature osteoclasts adhering to the bone surface tightly, secreting proteases and protons that degrade its matrix [12, 13], with excessive osteoclastogenic activity leading to pathological bone loss.

Classical and dual-specificity sub-families of the protein tyrosine phosphatases (PTPs) such as SHP1, SHP2, cyt-PTPe, and PTPRO are known to play key roles in the regulation of osteoclast differentiation [13]. Phosphatase of regenerating liver 2 (PRL2), also known as PTP4A2, is above the 90 percentile of genes that are

[1]Department of Immunology and Microbiology, Shanghai Institute of Immunology, Shanghai Jiao Tong University School of Medicine, Shanghai 200025, China. [2]Department of Rheumatology, Guanghua Hospital Affiliated to Shanghai University of Traditional Chinese Medicine, Shanghai 200052, China. [3]Key Laboratory of Cell Differentiation and Apoptosis of Chinese Ministry of Education, Department of Pathophysiology, Shanghai Jiao Tong University School of Medicine, Shanghai 200025, China. [4]Department of Oral and Cranio-Maxillofacial Surgery, Shanghai Ninth People's Hospital, Shanghai Jiao Tong University School of Medicine, Shanghai 200011, China. [5]Yangzhi Rehabilitation Hospital (Sunshine Rehabilitation Center), Tongji University School of Medicine, Shanghai 201619, China. [6]Key Laboratory of Parasite and Vector Biology, Ministry of Health, China; School of Global Health, Chinese Center for Tropical Diseases Research, Shanghai Jiao Tong University School of Medicine, Shanghai 200025, China. [7]These authors contributed equally: Qi Li, Tao Yue. ✉email: guangjie_chen@163.com; zjwang@sjtu.edu.cn

Edited by D Rubinsztein

Received: 10 January 2022 Revised: 19 September 2022 Accepted: 20 September 2022
Published online: 1 October 2022

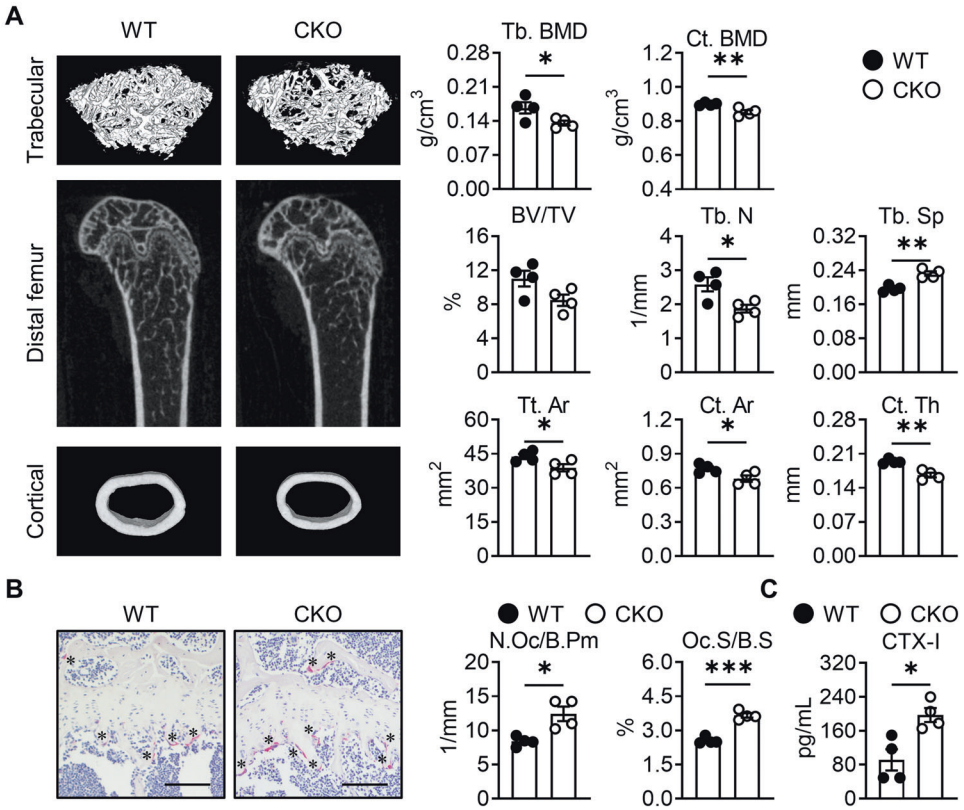

Fig. 1 PRL2 deficiency decreases bone mass and enhances the number of osteoclasts in vivo. A Representative micro-computed tomography (micro-CT) femoral images (left panel) of 12-week-old male *Ptp4a2*$^{fl/fl}$ mice (referred to as WT) and *Ptp4a2*$^{fl/fl}$*LysM*$^{Cre+}$ mice (referred to as CKO). Quantification of trabecular bone mineral density (Tb. BMD), cortical bone mineral density (Ct. BMD), trabecular bone volume/tissue volume (BV/TV), trabecular number (Tb. N), trabecular separation (Tb. Sp), total cross-sectional area (Tt. Ar), cortical bone area (Ct. Ar), and cortical thickness (Ct. Th) in femur tissues (right panel). ($n = 4$ images taken in total, one image from each of four mice). **B** Representative images of tibia tissues stained for TRAP (left panel) from WT and CKO 12-week-old male mice. Asterisks representative of TRAP-positive osteoclasts. Quantification of the number of osteoclasts/bone perimeter (N. Oc/B. Pm) and the osteoclast surface/bone surface (Oc. S/B. S) in tibia tissues (right panel). ($n = 4$ images taken in total, one image from each of four mice, scale bar, 100 μm). **C** Serum C-terminal telopeptide for type I collagen (CTX-I) levels in WT and CKO 12-week-old male mice ($n = 4$ per group). The data are shown as the mean ± s.e.m., $^{*}P < 0.05$, $^{**}P < 0.01$, $^{***}P < 0.005$, unpaired two-tailed Student's *t*-test.

the most strongly expressed in osteoclasts [13], but its role in osteoclastogenesis is unknown. PRL2 myeloid cell conditional knockout mice (*Ptp4a2*$^{fl/fl}$*LysM*$^{Cre+}$ mice, CKO) are born and develop normally, and have similar body size, blood, spleen, and bone marrow cellularity compared to their wild-type littermates (*Ptp4a2*$^{fl/fl}$ mice, WT) [14]. However, we found that adult PRL2 CKO mice have decreased bone mineral density and increased number of osteoclasts. Since PRL2 senses oxidative stress via highly reactive cysteine residues and is rapidly degraded during inflammation [14, 15], we hypothesized that PRL2 acts as an inflammation sensor and osteoclast modulator in inflammatory bone diseases.

In this study, we reveal the role of PRL2 in osteoclastogenesis during normal physiology, as well as in bone-associated pathology. In response to inflammatory oxidative stress, oxidized PRL2 is rapidly degraded via HSC70 mediated endosomal microautophagy (eMI) and chaperone-mediated autophagy (CMA), contributing significantly to inflammation-induced osteoclast hyperactivation and bone destruction, while treatment with the lysosome inhibitor hydroxychloroquine (HCQ) blocks such inflammation-induced PRL2 degradation and bone destruction. These findings demonstrate that PRL2 is a novel regulator in osteoimmunology and inhibition of HSC70 mediated autophagic degradation of PRL2 may offer new therapeutic tools for the treatment of inflammatory bone disease.

RESULTS

PRL2 deficiency decreases bone mass and enhances the number of osteoclasts in mice

To determine whether loss of PRL2 affected bone homeostasis in vivo, we isolated femora from 12-week-old PRL2 WT and myeloid cell conditional knockout (CKO) mice. Micro-computed tomography (μCT) analyses revealed that PRL2 deficiency resulted in a decrease of bone mass, and reduction in trabecular and cortical bone mineral density (Tb. BMD and Ct. BMD), trabecular number (Tb. N), total cross-sectional area (Tt. Ar), cortical bone area (Ct. Ar), and cortical thickness (Ct. Th) compared to the WT littermates. In contrast, trabecular separation (Tb. Sp) increased in PRL2 CKO mice (Fig. 1A) and more TRAP-positive osteoclasts (Fig. 1B) were found on the surface of tibia in PRL2 CKO mice. Histomorphometric analysis demonstrated a significant increase in the number of osteoclasts/bone perimeter (N. Oc/B. Pm) and osteoclast surface/bone surface (Oc. S/B. S) in PRL2 CKO mice compared to WT littermates (Fig. 1B). Serum C-terminal telopeptide for type I collagen (CTX-I), a bone resorption marker, was also increased in CKO mice compared to WT littermates (Fig. 1C). Moreover, PRL2 total knockout mice (*Ptp4a2*$^{fl/fl}$*E2a*$^{Cre+}$) exhibited lower bone mass than their wild-type littermates (Supplementary Fig. 1A, B). To determine whether the decreased bone mass is associated with bone formation, PRL2 total knockout mice, heterozygote mice (*Ptp4a2*$^{fl/+}$*E2a*$^{Cre+}$, HET), and their WT littermates were injected intraperitoneally with calcein, respectively.

There was no difference in the mineral apposition rate (MAR) among the three groups (Supplementary Fig. 1C). These results suggested that osteoclast hyperactivation was the main reason for the low bone mass observed in PRL2 CKO and total knockout mice.

PRL2 deficiency enhances osteoclast differentiation ability and bone resorptive capacity of osteoclasts in vitro

We next examined the role of PRL2 in osteoclast differentiation in vitro. Although there was no difference in *Rank* expression, cell survival or proliferation between WT and PRL2 KO cells in response to RANKL or M-CSF treatment (Supplementary Fig. 2), RANKL treatment resulted in notably greater osteoclast (tartrate-resistant acid phosphatase positive multinuclear cells, $TRAP^+$ MNCs) numbers in bone marrow monocytes (BMMs) from PRL2 CKO mice than from control mice (Fig. 2A). The expressions of the classic RANKL signaling mediators such as *Nfatc1*, *Ctsk*, *Mmp9*, and *Acp5*, were significantly increased in PRL2 KO osteoclasts in comparison to WT cells (Fig. 2B). Moreover, PRL2 deficient osteoclasts expressed higher protein levels of NFATc1 than WT cells (Fig. 2C). Besides primary murine monocytes, similar results were observed in PRL2 KO osteoclast precursor RAW 264.7 cells and control cells (Fig. 2D, E). We also compared the bone resorption ability between WT and PRL2 deficient osteoclasts. When seeded on the hydroxyapatite-coated Osteo Assay Surface plates, osteoclasts lacking PRL2 resorbed more than WT cells (Fig. 2F), confirming that the loss of PRL2 enhanced resorption activity in osteoclasts. Therefore, PRL2 could inhibit RANKL-induced osteoclast differentiation and function in vitro.

PRL2 affects the canonical RANK-signaling pathway via RAC1 and ROS

Our previous work has demonstrated that PRL2 binds to GTPase Rac and regulates ROS production in innate immune cells [14]. Since ROS are important components in the regulation of the differentiation of osteoclasts, we investigated whether PRL2 regulates ROS through its action on Rac1 in RANKL stimulated osteoclast precursors. As shown in Fig. 3A, RANKL treatment induced more activation of Rac GTPase in primary PRL2 KO BMMs compared to control cells. In response to RANKL stimulation, osteoclast precursors exhibited a transient and fast increase in ROS and PRL2 KO cells generated more ROS than WT cells (Fig. 3B, C). Furthermore, PRL2 deficiency promoted RANKL-induced MAPK and NF-κB signaling by increasing the phosphorylation of JNK, P38, ERK1/2 and NF-κB inhibitor-α (IκBα) (Fig. 3D). RAW 264.7 cells data were consistent with that of BMMs (Supplementary Fig. 3). Conversely, the elevated ROS production and NFATc1 expression in PRL2 KO cells reverted to the levels of WT cells following overexpression of PRL2 or dominant-negative Rac1 (T17N) in these cells (Fig. 3E–H).

Oxidative stress triggers rapid degradation of PRL2 by CMA and eMI

During inflammation PRL2 protein is oxidized and degraded rapidly [15]. Consistent with our previous observation, protein levels of PRL2 in BMMs or RAW 264.7 cells were significantly decreased with increasing concentrations of hydrogen peroxide (H_2O_2) and this effect was not associated with new protein synthesis (Fig. 4A and Supplementary Fig. 4A). To further elucidate the mechanism leading to PRL2 degradation in response to oxidative stress, BMMs and RAW 264.7 cells were cultured for 1 h in the presence of MG-132 to inhibit proteasomes, or hydroxychloroquine (HCQ) to inhibit lysosomes. The cells were then treated with different doses of H_2O_2. Results showed that protein levels of PRL2 were comparable with MG-132 or HCQ treatment under normal condition (Supplementary Fig. 4B). Inhibiting proteasomes did not prevent H_2O_2-induced PRL2 degradation, whereas HCQ blocked the degradation (Fig. 4B and Supplementary Fig. 4C). Confocal analysis revealed co-localization of PRL2 and lysosome-associated membrane protein1 (LAMP1), and the co-localization was enhanced under oxidative stress, further strengthening the evidence for PRL2 lysosomal degradation (Fig. 4C).

Endogenous protein lysosomal degradation occurs mainly via three forms of autophagy, macroautophagy, chaperone-mediated autophagy (CMA), and endosomal microautophagy (eMI) [16]. Hence, we determined the effects of the different types of autophagy on PRL2 degradation. First, we used Torin1 to induce macroautophagy in $Atg5^{-/-}$ mouse embryonic fibroblasts (MEFs), which lack the essential autophagy-related gene resulting in the lack of LC3-II conjugation (no autophagosome formation). Torin1 treatment stimulated macroautophagy, causing significantly increased LC3-II lipidation, while no such macroautophagic response were observed in $Atg5^{-/-}$ MEFs. However, the protein levels of PRL2 were comparable in $Atg5^{+/+}$ and $Atg5^{-/-}$ MEFs, even after Torin1 treatment (Supplementary Fig. 4D). We also used 3-methyladenine (3-MA), a well-known macroautophagy blocker, to inhibit macroautophagy in osteoclast precursors. As shown in Fig. 4D, 3-MA blocked LC3 convention in BMMs, but it did not block H_2O_2-induced PRL2 degradation. In addition, we analyzed the macroautophagy flux in the presence or absence of HCQ. Results showed that the levels of LC3-II increased in the presence of HCQ (Supplementary Fig. 4E). Above results suggested that oxidative stress induced PRL2 degradation is not primarily through macroautophagy. We next analyzed the effects of eMI and CMA on PRL2 degradation by siRNA silencing of *Vsp4a* and *Lamp2a*, respectively. To exclude eMI in PRL2 degradation, knockdown of *Vps4a* is a common strategy [17]. The most selective way to block CMA is through genetic knockdown of *Lamp2a*, since other components involved in CMA are also shared by other cellular processes [18]. Knockdown of either *Vsp4a* or *Lamp2a* significantly accumulated PRL2 (Supplementary Fig. 4F–H). Moreover, H_2O_2-induced PRL2 degradation was blocked in *Vsp4a* and *Lamp2a* knockdown cells (Fig. 4E, F and Supplementary Fig. 4I, J). Taken together, these observations suggested that the reduction of PRL2 under oxidative stress was due to CMA or eMI rather than macroautophagy.

In addition, to access which pool/form of PRL2 is degraded by CMA or eMI, we performed additional experiments using truncated PRL2 which has no CAAX motif and cannot be prenylated [19]. Results showed both cytosol and prenylated PRL2 can be degraded via CMA or eMI (Supplementary Fig. 4K). We also verified whether CMA is activated under oxidative stress in osteoclast progenitors using a photoactivated KFERQ-PA-mCherry1 reporter [18, 20]. As indicated in Supplementary Fig. 4L, there were more red fluorescent puncta in RAW 264.7 cells with H_2O_2 treatment, suggesting CMA activity was enhanced under oxidative stress.

PRL2 bears a KFERQ-like motif and binds directly to HSC70 for its autophagic degradation

In order to identify PRL2-interacting proteins, we performed large-scale co-immunoprecipitation (co-IP) and mass spectrometry screenings using RAW 264.7 cells. Among the peptides identified, ten originated from the Heat shock cognate 71 kDa protein (HSC70), also known as HSPA8, which is a chaperone protein participating in CMA or eMI [17, 21]. Thus, we tested whether PRL2 interacts with HSC70. We undertook 3 complementary approaches: First, we co-overexpressed HA-tagged HSC70 and Myc-tagged PRL2 in HEK293T cells. By co-IP analyses, we found that PRL2 interacted with HSC70 (Fig. 4G). The binding ability of PRL2 to HSC70 was enhanced under oxidative stress (Supplementary Fig. 5A). Second, we overexpressed Myc-tagged PRL2 in RAW 264.7 cells and analyzed the co-localization of PRL2 with endogenous HSC70 in basal state and in oxidative stress using immunofluorescence. Co-localization of PRL2 with HSC70 was increased when cells were under oxidative stress (Fig. 4H). Similar results were obtained when endogenous LAMP2A was

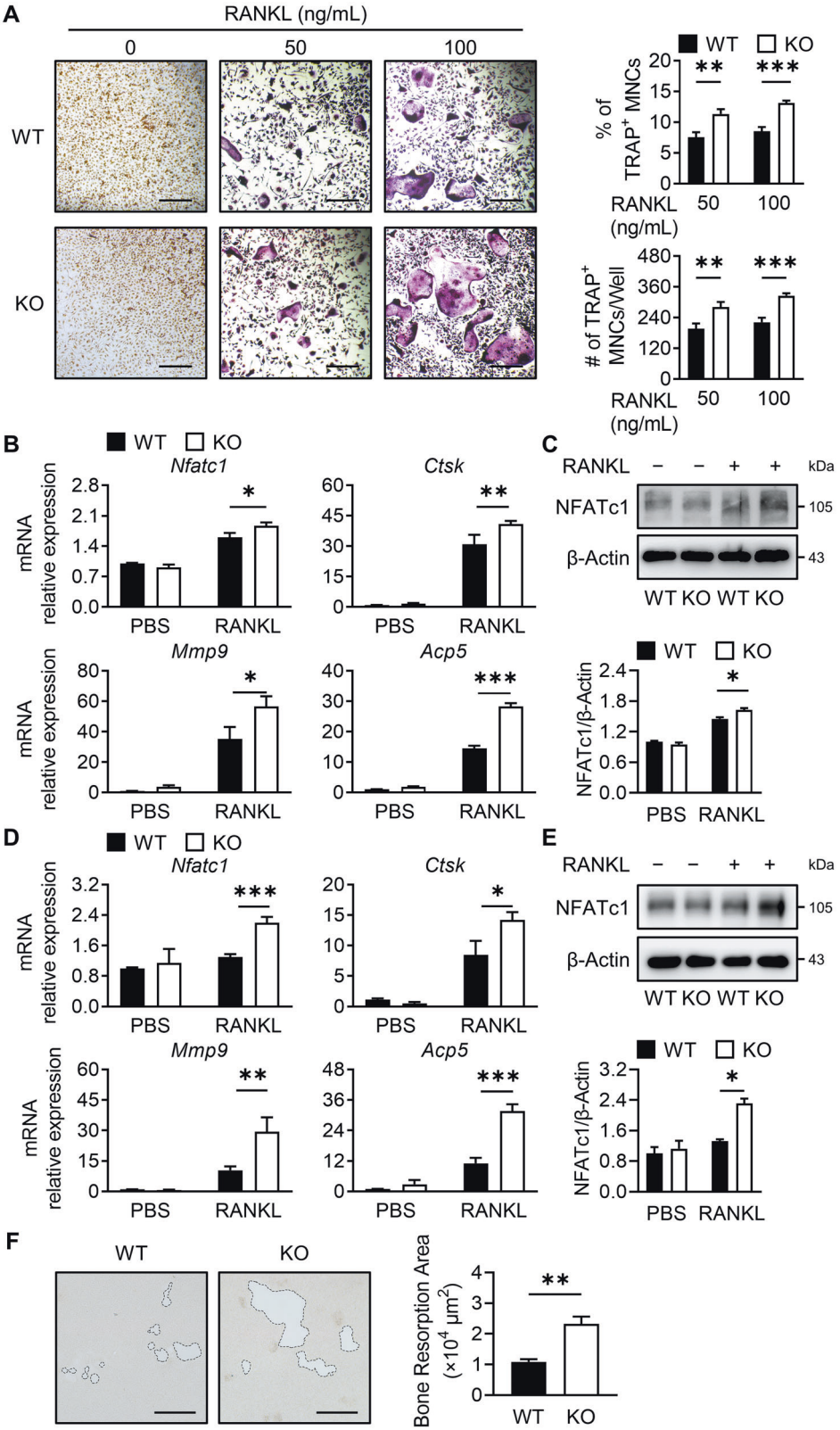

stained to examine PRL2-HSC70 co-localization in lysosomes of RAW 264.7 cells (Supplementary Fig. 5B). Consistent results were observed in HEK293T cells (Supplementary Fig. 5C, D). Third, we tested whether PRL2 and HSC70 directly interacted with each other. Prokaryotic recombinant His-tagged PRL2 proteins and GST-tagged HSC70 proteins were expressed and purified. After mixing them together, we found that PRL2 physically associated with HSC70, indicating that the two proteins directly bound to each other (Fig. 4l). Moreover, oxidized PRL2 displayed a much stronger interaction with HSC70 than reduced PRL2, suggesting

Fig. 2 PRL2 deficient monocytes and macrophages have increased osteoclastogenic capacity in vitro. A Representative TRAP staining images (left panel) of BMMs isolated from *Ptp4a2*$^{fl/fl}$ mice (referred to as WT) and *Ptp4a2*$^{fl/fl}$*LysM*$^{Cre+}$ mice (referred to as KO) stimulated with M-CSF and indicated concentrations of RANKL. Percentage (%) of TRAP-positive multinucleated cells (TRAP$^+$ MNCs) and number (#) of TRAP$^+$ MNCs per well (right panel). (Scale bar, 100 μm). **B** Transcript levels of *Nfatc1*, *Ctsk*, *Mmp9*, and *Acp5* in WT and KO BMMs with or without RANKL for 4 days. **C** Representative immunoblot images (upper panel) and quantification of protein levels of NFATc1 (lower panel) in WT and KO BMMs with or without RANKL for 2 days. **D** Transcript levels of *Nfatc1*, *Ctsk*, *Mmp9*, and *Acp5* in WT and *Ptp4a2* knockout (referred to as KO) RAW 264.7 cells with or without RANKL for 2 days. **E** Representative immunoblot images (upper panel) and quantification of protein levels of NFATc1 (lower panel) in WT and KO RAW 264.7 cells with or without RANKL for 2 days. **F** Resorption pit assay (left panel) and quantification of bone resorption area (right panel) of WT and KO mature osteoclasts. (Scale bar, 100 μm) The data are representative of two or four independent experiments (biological replicates) and shown as the mean ± s.e.m., $^*P < 0.05$, $^{**}P < 0.01$, $^{***}P < 0.005$, unpaired two-tailed Student's *t*-test.

that PRL2 oxidation might increase its interaction with HSC70 (Fig. 4J). We also tested C46S/C101S mutant of PRL2, which cannot be oxidized and form an intramolecular disulfide bond [15]. Following exposure to H_2O_2, C46S/C101S mutant of PRL2 decreased less as compared with WT PRL2 (Supplementary Fig. 5E). Importantly, C46S/C101S mutant showed less interaction with HSC70 than WT PRL2 (Supplementary Fig. 5F).

HSC70 binds directly to a KFERQ-like motif in the cargo protein for its autophagic targeting [21, 22]. Inspection of the PRL2 amino acid sequence revealed three potential HSC70 binding motifs, ^{83}NLLKT^{87}, ^{84}LLKTK^{88}, and ^{86}KTKFR^{90} (Fig. 4K). We replaced N83L84, K86T87, and T87K88 with alanine and examined the interaction of each mutant with HSC70. Neither the N83A/L84A mutant nor the T87A/K88A mutant decreased the interaction with HSC70, while the K86A/T87A mutant significantly reduced its interaction with HSC70 (Fig. 4L). Consistent with this finding, the K86A/T87A mutant was more resistant to oxidative stress-induced protein degradation than the wild-type PRL2 or the other two mutants (Fig. 4M and Supplementary Fig. 5G), providing additional support for HSC70 mediated degradation of PRL2.

Degradation of PRL2 contributes to osteolysis in inflammatory bone diseases

To address the pathophysiological role of PRL2 in regulating inflammatory osteolysis in vivo, we subcutaneously injected LPS into WT and PRL2 CKO mouse calvaria to induce inflammatory osteolysis. As shown in Fig. 5A, the administration of LPS caused significant bone destruction in the calvaria. Histomorphometric analysis of the calvaria revealed that both N. Oc/B. Pm and Oc. S/B. S in LPS-injected PRL2 CKO mice increased markedly compared to WT mice (Fig. 5B).

Second, we induced K/B×N serum transfer-induced arthritis (STIA) in WT C57BL/6 mice, and examined the relationship between PRL2 levels and the progression of inflammatory arthritis. After arthritis induction by injection of K/B×N serum, the mice showed typical signs and symptoms of arthritis, with increasing ankle thickness and clinical indices as depicted in Fig. 5C. The degree of bone erosion was striking in mice sacrificed at day 15 and accompanied by markedly enhanced number of osteoclasts in the cortical bone (Fig. 5D), increased serum CTX-I levels (Fig. 5E) and increased oxidative stress levels in blood (Fig. 5F), while PRL2 protein levels in leukocytes were significantly reduced in arthritic mice (Fig. 5G). Meanwhile, the transcript levels of PRL2 were similar in arthritis and control mice (Supplementary Fig. 6A). We further measured the protein levels of PRL2 in different peripheral cell subsets using flow cytometry and found that PRL2 levels were comparable in B and T lymphocytes (B220$^+$ and CD3$^+$), but decreased in myeloid cells (CD11b$^+$) from day 9. Dramatically reduced PRL2 protein levels were observed in CD11b$^+$ myeloid cells, and its main subsets monocytes (Ly-6C^{hi}Ly-6G$^-$) and neutrophils (Ly-6C^{lo}Ly-6G$^+$) at day 15 (Fig. 5H).

Finally, we compared the protein levels of PRL2 between 30 RA patients and 17 healthy controls. The results were consistent with the findings in the STIA model. There was no difference in transcription levels of PRL2 between peripheral blood mononuclear cells (PBMCs) from RA patients and healthy controls (Supplementary Fig. 6B). However, PBMCs from RA patients showed enhanced ROS levels and significantly reduced PRL2 protein levels in CD14$^+$ monocytes (Fig. 5I–K). These results suggested that lower PRL2 protein levels in osteoclast precursors (mouse Ly-6C^{hi} monocytic population and human CD14$^+$ monocytes) was correlated with severity of bone erosion.

HCQ blocks PRL2 lysosomal degradation and ameliorates bone loss during inflammation

Evidence suggests that treatment with HCQ can delay or prevent bone destruction in various rheumatic diseases [23]. Since HCQ blocks PRL2 lysosomal degradation in vitro, we examined the potential relationship between HCQ and PRL2 in osteoclastogenesis and bone loss. In the STIA model, there was no difference between arthritic mice in clinical score or joint thickness when treated with normal saline (NS) or HCQ (Fig. 6A). However, N. Oc/B. Pm and Oc. S/B. S in arthritic mice treated with HCQ were dramatically decreased (Fig. 6B), as were the levels of serum CTX-I (Fig. 6C). And although HCQ treatment had no effect on intracellular ROS or transcription levels of PRL2 in peripheral blood cells, PRL2 protein levels in leukocytes were partially reversed in arthritic mice after HCQ treatment (Fig. 6D, E and Supplementary Fig. 6C). Likewise, PRL2 protein levels in myeloid cells, but not in B or T lymphocytes, were reversed by HCQ treatment (Fig. 6F), suggesting that the protective effect of HCQ on mouse arthritis was due to the capacity of HCQ to block PRL2 degradation and osteoclast precursor activation.

DISCUSSION

Chronic inflammation results in osteoclast-driven bone erosion, which is a key outcome correlating with disease severity and functional deterioration in inflammatory bone diseases such as RA, systemic lupus erythematosus and inflammatory bowel diseases [24, 25]. A better understanding of the molecular mechanism involved in bone loss, particularly in the context of inflammation, is essential for the development of new therapies to halt bone erosion. Here, we provide evidences that PRL2 serves as a molecular link between inflammation and bone erosion through its ability to regulate osteoclastogenesis. This conclusion is based on the following observations: (a) the absence of PRL2 in myeloid cells leads to an osteopenia phenotype and promotes LPS-induced inflammatory osteolysis in mice, (b) PRL2 negatively regulates osteoclast differentiation and bone resorptive capacity in vitro, (c) oxidative stress leads to PRL2 oxidation and degradation via HSC70 mediated eMI and CMA, (d) in arthritic mice and RA patients, reduced PRL2 protein levels in peripheral osteoclast precursors correlates with bone destruction and increased oxidative stress in the cells, and (e) the inhibition of autophagy (using HCQ) blocks PRL2 degradation and inflammatory bone destruction in vivo.

Bone tissue is formed and maintained by the coordinated actions of mesenchymal-derived osteoblasts and hematopoietic-derived osteoclasts. Bone marrow cells with a deletion of PRL2 expression in

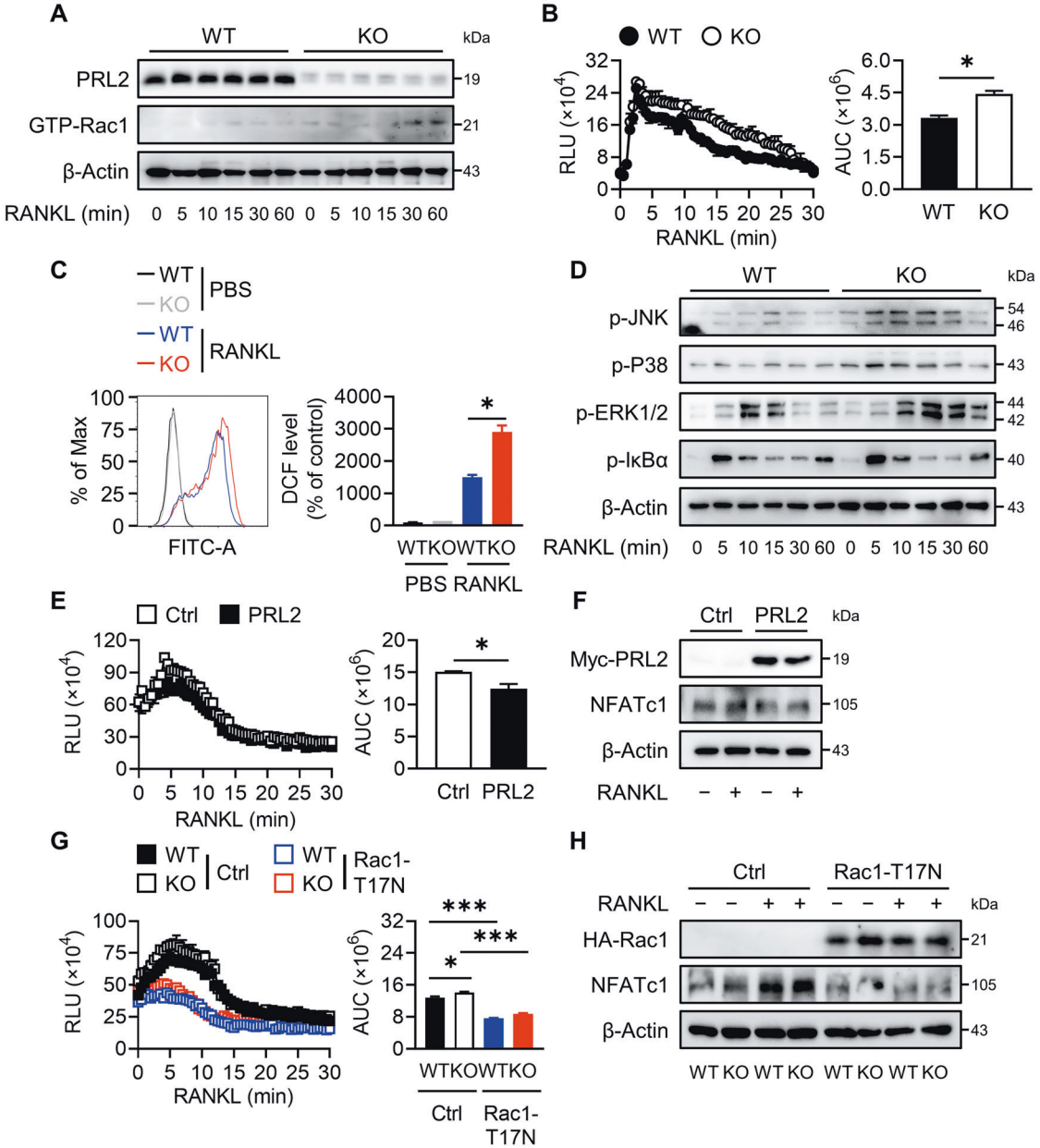

Fig. 3 PRL2 deficiency enhances the canonical RANK-signaling pathway via Rac1 and ROS. A Representative immunoblot images for GTP-Rac1 in BMMs isolated from *Ptp4a2*$^{fl/fl}$ mice (referred to as WT) and *Ptp4a2*$^{fl/fl}$*LysM*$^{Cre+}$ mice (referred to as KO) stimulated with RANKL for the indicated times. **B** Dynamic curves of ROS production (left panel) and area under curve (AUC, right panel) in WT and KO BMMs stimulated with RANKL (RLU, relative light unit). **C** Mean fluorescence intensity (MFI) of DCF-DA in WT and KO BMMs with or without RANKL for 30 min (left panel). Quantification of relative DCF level, normalized by WT BMMs without RANKL (right panel). **D** Representative immunoblot images for phosphorylated forms of signaling proteins in WT and KO BMMs stimulated with RANKL for the indicated times. **E** Dynamic curves of ROS production (left panel) and AUC (right panel) in *Ptp4a2* knockout RAW 264.7 cells (referred to as KO) replenished with control (Ctrl) or PRL2 with RANKL. **F** Representative immunoblot images for NFATc1 in KO RAW 264.7 cells replenished with Ctrl or PRL2 with or without RANKL for 2 days. **G** Dynamic curves of ROS production (left panel) and AUC (right panel) in WT and KO RAW 264.7 cells replenished with Ctrl and Rac1-T17N with RANKL. **H** Representative immunoblot images of NFATc1 in WT and KO RAW 264.7 cells replenished with Ctrl and Rac1-T17N with or without RANKL for 2 days. The data are representative of two or three independent experiments (biological replicates), and for **B**, **C**, **E**, and **G**, the data are shown as the mean ± s.e.m., *$P < 0.05$, **$P < 0.01$, ***$P < 0.005$, unpaired two-tailed Student's *t*-test.

myeloid cells, obtained by crossing a *flox* allele of PRL2 with *LysM*$^{cre+}$ mice, showed significantly increased capacity to form osteoclasts in vitro. In addition, such PRL2-deficient osteoclasts exhibited significantly increased ROS production and enhanced expression of the key osteoclastogenic transcription factor NFATc1. Histomorphometric studies revealed increased number of osteoclasts in these mice in vivo, and affected overall bone mass. Taken together, these findings suggest that PRL2 down-regulates the signaling process triggered by RANKL in osteoclasts and that PRL2 may act as a novel inhibitor of RANKL-mediated osteoclastogenesis. However, the role of PRL2 in osteoblasts remains unknown. Data from the International Mouse Phenotyping Consortium (IMPC) indicate that PRL2 gene total knockout mice (*Ptp4a2*$^{em1(IMPC)Tcp}$) have abnormal bone structure and shorter tibia, while our PRL2 total knockout mice (*Ptp4a2*$^{fl/fl}$*E2a*$^{Cre+}$) exhibited lower bone mass than their wild-type littermates. These bone phenotypes suggest that the

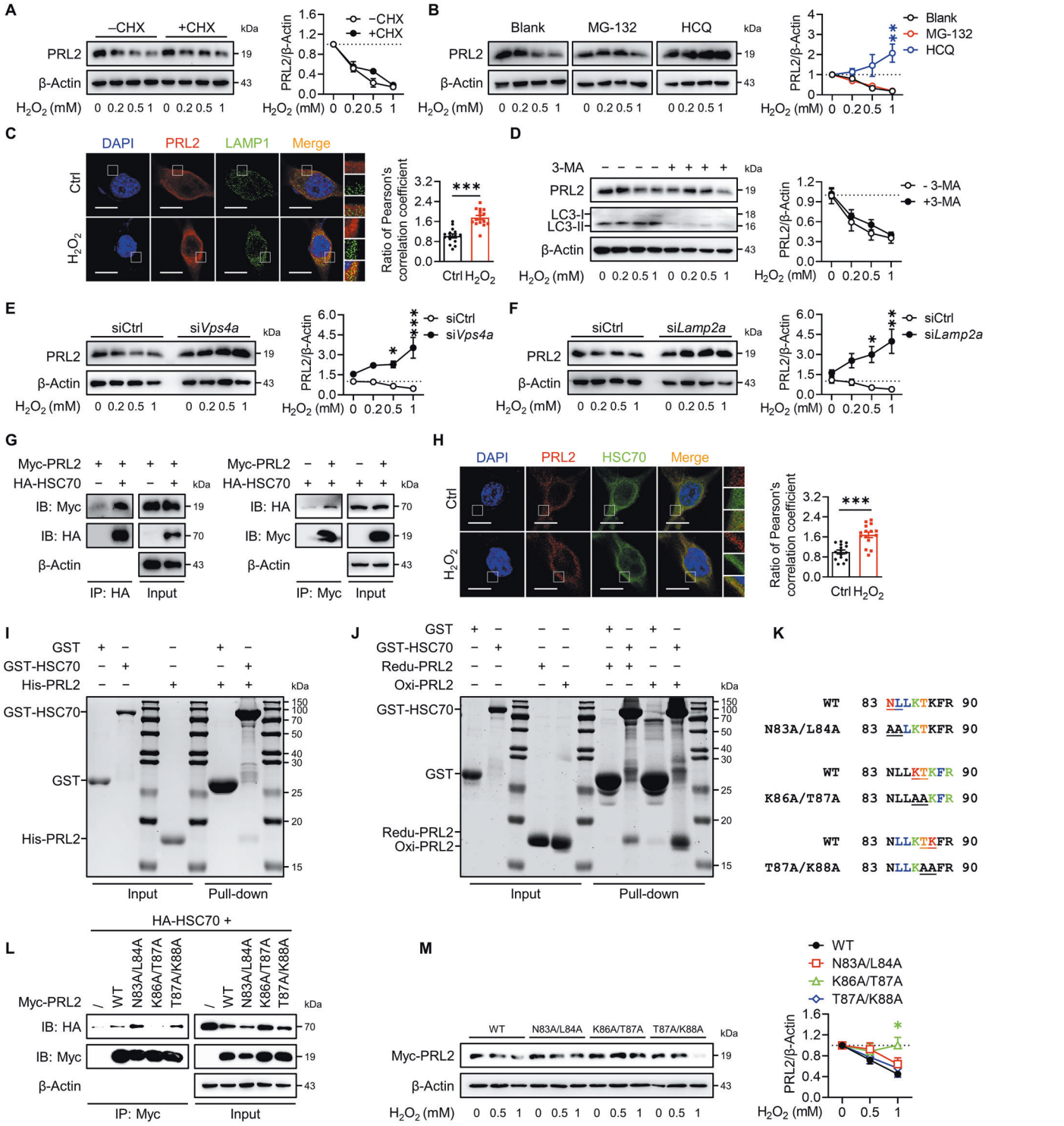

general attributes of PRL2 deficiency in the body are towards bone degradation. Moreover, data from Genome-Wide Association Studies (GWAS) show that a single nucleotide polymorphism (SNP) within the PTP4A2 gene (rs10914505, and rs61516782) is correlated with human body height [26, 27]. Taken together, the above evidence suggest that PRL2 is involved in the balance of bone metabolism.

Both eMI and CMA involve the identification of misfolded proteins by HSC70 [28]. Proteins degraded by eMI or CMA have a pentapeptide with the consensus sequence KFERQ (Lys-Phe-Glu-Arg-Gln) and approximately one-third of soluble cytosolic proteins bear a KFERQ-like motif. In addition, post-translational modifications can expand the number of potential substrates. E can be replaced with phosphorylated S, T or Y, and Q can be replaced with acetylated K, which both occur in PRL2 [21]. In this study, we identified that PRL2 possesses a KFERQ-like motif, ^{86}KTKFR^{90}, which facilitates PRL2, and in particular oxidized PRL2, binding to HSC70 and undergoing degradation via the lysosomal pathway. It is a novel molecular mechanism that regulates PRL2 protein stability under oxidative stress. Post-translational modifications can modulate protein stability, as well as affect its subcellular

Fig. 4 PRL2 bearing KFERQ-like motif is recognized by HSC70 and degraded via lysosomal pathway under oxidative stress. **A** Representative immunoblot images (left panel) and quantification of protein levels of PRL2 (right panel) in 10 μg/mL cycloheximide (CHX) pre-treated RAW 264.7 cells treated with the indicated concentrations of H_2O_2 for 30 min. Cells were pre-treated with CHX for 1 h. **B** Representative immunoblot images (left panel) and quantification of protein levels of PRL2 (right panel) in 20 μM MG-132 or 50 μM hydroxychloroquine (HCQ) pre-treated RAW 264.7 cells treated with the indicated concentrations of H_2O_2 for 30 min. Cells were pre-treated with MG-132 or HCQ for 1 h. **C** Representative confocal images (left panel) and quantification (right panel) for subcellular localization of PRL2 in lysosome (stained with LAMP1) in RAW 264.7 cells with or without 1 mM H_2O_2 for 5 min. (Scale bar, 10 μm). **D** Representative immunoblot images (left panel) and quantification of protein levels of PRL2 (right panel) in 1 mM 3-methyladenine (3-MA) pre-treated BMMs treated with the indicated concentrations of H_2O_2 for 30 min. Cells were pre-treated with 3-MA for 6 h. **E** Representative immunoblot images (left panel) and quantification of protein levels of PRL2 (right panel) in *Vsp4a* knockdown RAW 264.7 cells treated with the indicated concentrations of H_2O_2 for 30 min. **F** Representative immunoblot images (left panel) and quantification of protein levels of PRL2 (right panel) in *Lamp2a* knockdown RAW 264.7 cells treated with the indicated concentrations of H_2O_2 for 30 min. **G** Representative IP: HA images (left panel) and IP: Myc images (right panel) for the interaction between PRL2 and HSC70 in HEK293T cells. **H** Representative confocal images (left panel) and quantification (right panel) for the subcellular co-localization of PRL2 and HSC70 in RAW 264.7 cells with or without 1 mM H_2O_2 for 5 min. (Scale bar, 10 μm). **I** Representative GST-pulldown images for the interaction between purified PRL2 and HSC70 protein. **J** Representative GST-pulldown images for the interaction between purified oxidized or reduced PRL2 and HSC70 protein. **K** Amino acid sequence of wild-type PRL2 and the 3 mutants of the KFERQ-like motif. **L** Representative IP: Myc images for the interaction between wild-type PRL2, or the 3 mutants of the KFERQ-like motif, and HSC70 in HEK293T cells. **M** Representative immunoblot images (left panel) and quantification of protein levels of PRL2 (right panel) for wild-type PRL2, or the 3 mutants of the KFERQ-like motif in HEK293T cells treated with the indicated concentrations of H_2O_2 for 30 min. The data are representative of two or four independent experiments (biological replicates), and for **A**–**F**, **H**, and **M**, the data are shown as the mean ± s.e.m., $^*P < 0.05$, $^{**}P < 0.01$, unpaired two-tailed Student's *t*-test or one-way ANOVA followed by post hoc Tukey's test.

distribution, activity, or interactions with other proteins. PTP proteins are commonly susceptible to oxidation [29] and it has been reported that oxidation induces PRL2 to form an intramolecular disulfide bond between the catalytic cysteine Cys101 and the proximal Cys46 [15, 29, 30]. The formation of this intramolecular disulfide bond might alter the protein conformation and support better exposure of the pentapeptide (^{86}KTKFR^{90}) in order to be recognized by HSC70. There are 3 members of the PRL family, PRL1, PRL2, and PRL3. In humans, PRL1 and PRL2 share 87% homology, while PRL2 and PRL3 are 76% homologous [31]. PRL1 and PRL3 can form a similar intramolecular disulfide bond between the catalytic Cys49 and Cys104 as PRL2. However, there is no KFERQ-like motif between Cys49 and Cys104. Therefore, the above degradation mechanism and post-translational modification of PRL2 may be unique and specific, in order to ensure precise regulation of protein conformation and proteostasis.

CMA can be activated under oxidative stress and increased activity of this pathway, together with the higher susceptibility of oxidized proteins to be taken up by lysosomes, which may contribute to the efficient removal of oxidized proteins. In 2004, Kiffin reported that CMA induction of oxidative stress in rodents and culture cells increases the degradation of proteins via CMA [32]. Then, the effect of oxidative stress on CMA was extensively studied and confirmed by scholars using different methods [17, 18]. Such as, Koga et.al developed a photoconvertible fluorescent reporter and showed that H_2O_2 treatment results in an increase CMA activation [20]. In this study, our data demonstrated that oxidative stress can activate CMA in osteoclast progenitors, which promoted the degradation of oxidized PRL2 and osteoclastogenesis.

MATERIALS AND METHODS

Mice

PRL2 myeloid conditional knockout (*Ptp4a2*$^{fl/fl}$*LysM*$^{Cre+}$, CKO) mice, PRL2 total knockout (*Ptp4a2*$^{fl/fl}$*E2a*$^{Cre+}$, KO) mice, PRL2 heterozygote (*Ptp4a2*$^{fl/+}$*E2a*$^{Cre+}$, HET) mice, and their wild-type littermates (*Ptp4a2*$^{fl/fl}$, WT) on the C57BL/6 background have been described previously [14]. Wild-type C57BL/6 mice were purchased from Shanghai Laboratory Animal Center, Chinese Academy of Sciences. KRN T cell receptor transgenic mice maintained on a C57BL/6 background (K/B) were kindly provided by Fubin Li's Lab from Shanghai Jiao Tong University School of Medicine. NOD/Lt mice were purchased from GemPharmatech Co., Ltd (Strain ID No. N000235). Mice were housed under specific pathogen-free conditions and fed autoclaved food and water. All animal experiments were approved by the Institutional Animal Care and Use Committee (IACUC) of Shanghai Jiao Tong University School of Medicine (Project number A-2019-053, A-2019-069).

Human subjects

This study was approved by the Ethics Committee of Guanghua Hospital Affiliated to Shanghai University of Traditional Chinese Medicine (Project number 2021-K-46), and all subjects provided signed informed consent. This study has been registered at chictr.org.cn (ChiCTR2100046850). This study was performed in accordance with the Declaration of Helsinki. A total of 30 RA patients and 17 healthy controls were enrolled in this study. All patients who fulfilled the 1987 American College of Rheumatology (ACR) revised classification criteria for RA or the ACR/European League Against Rheumatism (EULAR) 2010 classification criteria for RA [33] were recruited from the Guanghua Hospital Affiliated to Shanghai University of Traditional Chinese Medicine from June 2021 to December 2021. The clinical characteristics of the RA patients and healthy controls were collected from their medical records and were summarized in Supplementary Table 1. Peripheral blood mononuclear cells (PBMCs) from patients and healthy controls were obtained from blood by density centrifugation at 800 g for 20 min at room temperature, using Lymphoprep™ (STEMCELL Technologies, Canada). After washing the cells twice with normal saline solution, PBMCs were harvested for further experiments.

Micro-computed tomography

Femurs collected from mice were fixed in 4% paraformaldehyde (PFA) and stored in 70% ethanol. Bone microstructure parameters including trabecular bone mineral density (Tb. BMD), bone volume/tissue volume ratio (BV/TV), trabecular number (Tb. N), trabecular separation (Tb. Sp), cortical bone mineral density (Ct. BMD), total cross-sectional area (Tt. Ar), cortical bone area (Ct. Ar), and cortical thickness (Ct. Th) were analyzed using Skyscan1176 (Huzbio Biotechnology Corp., Ltd., China) (Bruker, Belgium). The three-dimensional microstructures of femurs were imaged at a resolution of 9 μm (one slice) with an X-ray energy of 55 kVp, 170 μA, and an integration time of 200 ms.

Bone histomorphometric analysis

The tibias, calvarias or ankle joints of mice were prepared for bone histomorphometric analyses. In brief, bones were fixed in 4% PFA, decalcified with ethylene diamine tetraacetic acid (EDTA), and embedded in paraffin. Serial sections were stained with tartrate resistant acid phosphatase (TRAP). Sections were examined with an Olympus BX51 or IX71 microscope and data were acquired with the Olympus DP12 digital camera controlled by CellSens Standard software (Olympus, Japan). The number of osteoclast/bone perimeter (N. Oc/B. Pm) and osteoclast surface/bone surface (Oc. S/B. S) were calculated using Image Pro Plus software as described previously [34].

To analyze dynamic bone parameters, 4-week-old WT, HET and KO mice were injected intraperitoneally with 30 mg/kg calcein (Sangon Biotech, China) on 12 and 2 days prior to sacrifice. The mineral apposition rate (MAR) was quantified on unstained MMA-sections. Data were presented as described previously [35].

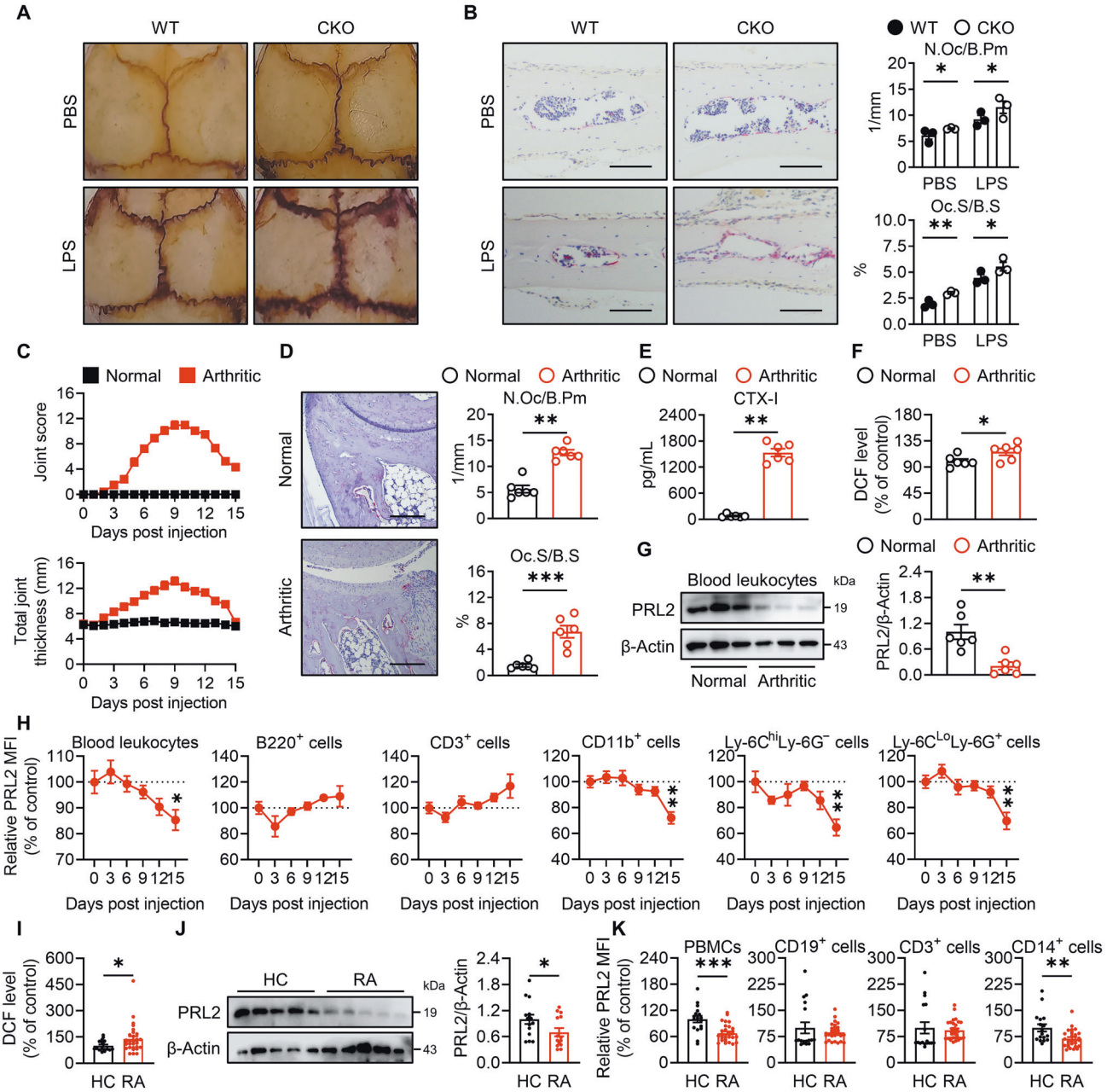

Fig. 5 PRL2 negatively regulates inflammatory bone diseases. A Representative TRAP staining images of *Ptp4a2*$^{fl/fl}$ mice (referred to as WT) and *Ptp4a2*$^{fl/fl}$*LysM*$^{Cre+}$ mice (referred to as CKO) with or without LPS treatment. ($n = 3$ images taken in total, one image from each of three mice). **B** Representative images of calvaria tissues stained for TRAP (left panel) from WT and CKO mice. Quantification of the number of osteoclasts/bone perimeter (N. Oc/B. Pm) and osteoclast surface/bone surface (Oc. S/B. S) in calvaria tissues (right panel) ($n = 3$ images taken in total, one image from each of three mice, scale bar, 100 μm). **C** Joint score and total joint thickness of normal and arthritic mice. ($n = 6$ per group). **D** Representative images of ankle joint tissues stained for TRAP (left panel) from normal and arthritic mice at day 15. Quantification of N. Oc/B. Pm and Oc. S/B. S in ankle joint tissues (right panel) ($n = 6$ images taken in total, one image from each of six mice, scale bar, 200 μm). **E** Serum C-terminal telopeptide for type I collagen (CTX-I) levels in normal and arthritic mice at day 15. ($n = 6$ per group). **F** Relative DCF levels in blood leukocytes from normal and arthritic mice at day 15, normalized to normal mice. ($n = 6$ per group). **G** Representative immunoblot images (left panel) and quantification of protein levels of PRL2 (right panel) in blood leukocytes from normal and arthritic mice at day 15. **H** Relative PRL2 mean fluorescence intensity (MFI) in blood leukocytes, B lymphocytes (B220$^+$), T lymphocytes (CD3$^+$), myeloid cells (CD11b$^+$), monocytes (Ly-6C^{hi}Ly-6G$^-$), and neutrophils (Ly-6C^{lo}Ly-6G$^+$) from arthritic mice at the indicated times, normalized to normal mice. ($n = 6$ per group). **I** Relative DCF level in peripheral blood mononuclear cells (PBMCs) from healthy controls (HC, $n = 17$) and RA patients ($n = 30$), normalized to HC. **J** Representative immunoblot images from 5 HC and 5 RA patients (left panel) and quantification of protein levels of PRL2 in PBMCs from HC and RA patients (right panel). **K** Relative PRL2 MFI in PBMCs, B lymphocytes (CD19$^+$), T lymphocytes (CD3$^+$), and monocytes (CD14$^+$) in HC ($n = 17$) and RA patients ($n = 30$), normalized to HC. The data are shown as the mean ± s.e.m., $^*P < 0.05$, $^{**}P < 0.01$, $^{***}P < 0.005$, unpaired two-tailed Student's *t*-test.

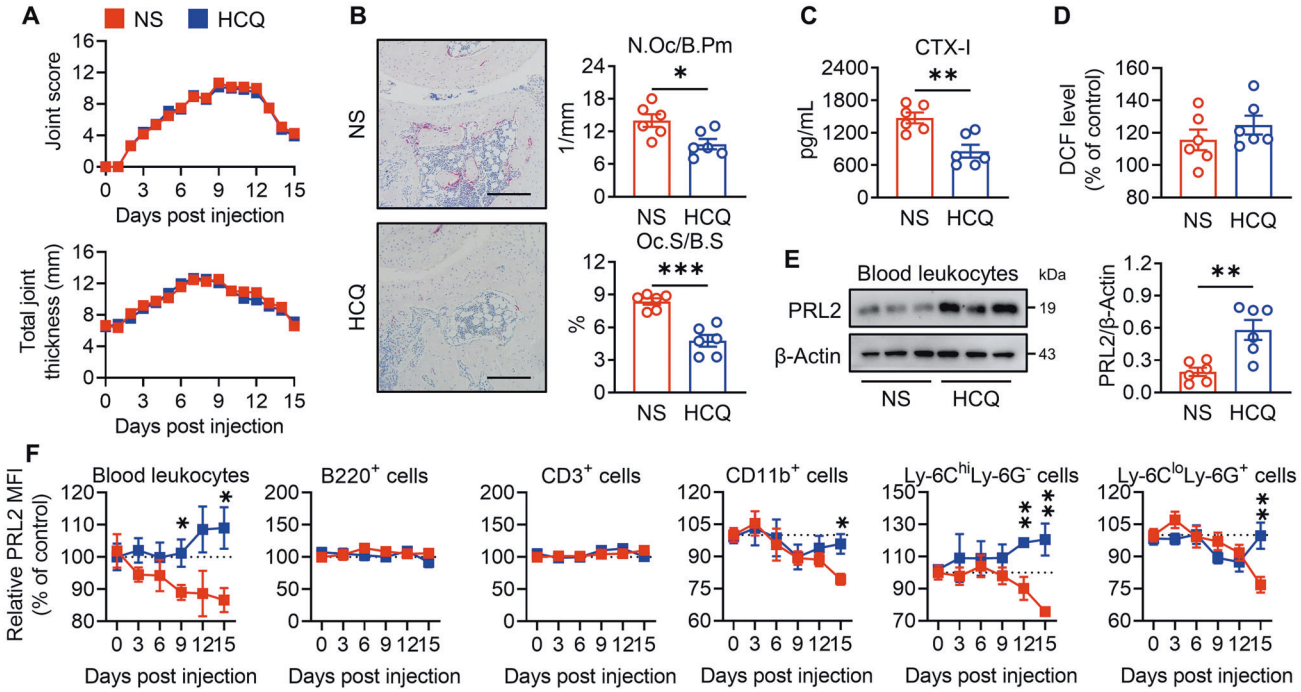

Fig. 6 HCQ blocks PRL2 degradation and ameliorates bone loss. A Joint score and total joint thickness of arthritic mice treated with normal saline (NS) or HCQ. ($n = 6$ per group). **B** Representative images of ankle joint tissues stained for TRAP (left panel) from arthritic mice treated with NS or HCQ at day 15. Quantification of the number of osteoclasts/bone perimeter (N. Oc/B. Pm) and osteoclast surface/bone surface (Oc. S/B. S) in ankle joint tissues (right panel). ($n = 6$ images taken in total, one image from each of six mice, scale bar, 200 μm). **C** Serum C-terminal telopeptide for type I collagen (CTX-I) levels in arthritic mice treated with NS or HCQ at day 15 ($n = 6$ per group). **D** Relative DCF level in blood leukocytes from arthritic mice treated with NS or HCQ at day 15, normalized to normal mice. ($n = 6$ per group). **E** Representative immunoblot images (left panel) and quantification of protein levels of PRL2 (right panel). in blood leukocytes from arthritic mice treated with NS or HCQ at day 15. **F** Relative PRL2 mean fluorescence intensity (MFI) of B lymphocytes ($B220^+$), T lymphocytes ($CD3^+$), myeloid cells ($CD11b^+$), monocytes ($Ly\text{-}6C^{hi}Ly\text{-}6G^-$), and neutrophils ($Ly\text{-}6C^{lo}Ly\text{-}6G^+$) from arthritic mice treated with NS or HCQ, normalized to normal mice at the indicated times ($n = 6$ per group). The data are shown as the mean ± s.e.m. $^*P < 0.05$, $^{**}P < 0.01$, $^{***}P < 0.005$, unpaired two-tailed Student's *t*-test.

ELISA

Blood was collected from mice and sera were stored at −80 °C. Serum C-terminal telopeptide for type I collagen (CTX-I) levels were analyzed using mouse ELISA kits (Elabscience, China) according to manufacturer's instructions.

Cell culture and transfection

Mouse primary femoral and tibial bone marrow cells were used for osteoclastogenesis. In brief, bone marrow cells were treated with 50 ng/mL murine M-CSF (R&D Systems, USA) in Minimum Essential Medium-α (Hyclone, USA) containing 10% heat-inactivated FBS, 2 mM L-glutamine, and 100 U/mL penicillin/streptomycin for 4 days in order to differentiate into bone marrow monocytes (BMMs), which are widely used as primary osteoclast precursors. BMMs were then further induced to mature osteoclasts with 50 ng/mL murine M-CSF and 100 ng/mL RANKL (R&D Systems, USA) for an additional 4 days, unless otherwise noted. TRAP staining was performed using a Leukocyte Acid Phosphatase kit (Sigma-Aldrich, USA) according to the manufacturer's instructions. Mature osteoclasts were defined as TRAP-positive multinucleated cells ($TRAP^+$ MNCs) with 3 or more nuclei.

Mouse embryonic fibroblasts (MEFs), murine RAW 264.7 (ATCC) and HEK293T cell lines (ATCC) were cultured in Dulbecco's Modified Eagle's Medium (Thermo Fisher Scientific, USA) containing 10% heat-inactivated FBS, 2 mM L-glutamine, and 100 U/mL penicillin/streptomycin. $Atg5^{+/+}$ and $Atg5^{-/-}$ MEFs, originally generated by N. Mizushima [36], were kindly provided by Qing Zhong's Lab from Shanghai Jiao Tong University School of Medicine. Transient transfections were performed using Attractene transfection reagent (QIAGEN, Germany) according to the manufacturer's instructions. Briefly, the day before transfection cells were seeded in plates at a density of 40% to 60% during transfection. The plasmid-Attractene or siRNA-Attractene mixture were added, the plates were gently mixed and placed in a 37 °C incubator overnight. The culture medium was changed after 12 h and the plates were incubated for another 24–48 h.

CRISPR/Cas9-mediated genome editing

Ptp4a2 sgRNA was designed using the online tool (zlab.bio/guide-design-resources), and the sgRNA sequence used was as follows: 5′-TGCACTG-CAACACAACAGCC-3′. lentiGuide-Puro-*Ptp4a2* plasmids were constructed by inserting *Ptp4a2* sgRNA into the *BsmB* I site of the lentiGuide-Puro vector (Addgene plasmid No. 52963). RAW 264.7 cells expressing Cas9 were kindly provided by Huabing Li's Lab from Shanghai Jiao Tong University School of Medicine and were transiently transfected with lentiGuide-Puro-*Ptp4a2* plasmids. Following transfection, cells were selected with 10 μg/mL puromycin for 2 weeks and the resistant population was determined by Western blot analysis.

Plasmid and siRNA construction

Myc-PRL2-pRK5, PRL2-pET302/NT-His and PRL2-C46S/C101S-pET302/NT-His plasmids were generated as described previously [14, 15]. HA-Rac1-T17N-pRK5 plasmid was obtained from Dr. YH Chen's lab and were generated as described previously [37]. HSC70-pIPHA2 plasmid was kindly provided by Bin Li's Lab from Shanghai Jiao Tong University School of Medicine. The HSC70 fragment digested with *BamH* I and *Xho* I was subcloned into a pGEX-4T-1 plasmid, and the HSC70-pGEX-4T-1 plasmid was generated for further experiments. KFERQ-like motif mutants (N83A/L84A, K86A/T87A, and T87A/K88A) of Myc-PRL2-pRK5 plasmid were generated by PCR-based site directed mutagenesis. All constructs and mutations were confirmed by DNA sequencing.

The siRNA specific for *Vps4a* and *Lamp2a* and scramble siRNA oligonucleotides were synthesized by Genomeditech Co., Ltd. The siRNA sequences are listed as below:

si*Vps4a*: 5′-UCAAAGAGAACCAGAGUGA-3′;
si*Lamp2a*: 5′-GACUGCAGUGCAGAUGAAG-3′.

RNA isolation and real-time quantitative PCR

Total RNA was extracted from cultured cells using the High Pure RNA Isolation Kit (Roche, Germany) in accordance with the manufacturer's

instructions. Mouse complementary DNA (cDNA) was reverse-transcribed with RevertAid First Strand cDNA Synthesis Kit (Invitrogen, USA) and real-time quantitative PCR was performed on a 7500 Fast Real-Time PCR System (Applied Biosystems, USA) using FastStart Universal SYBR Green Master Mix (Roche, Germany). Relative gene expression was normalized to *β-actin* (mouse) or *β-ACTIN* (human). Primer sequences are listed as below:

β-actin Forward: 5′-TCTGCTGGAAGGTGGACAGT-3′;
β-actin Reverse: 5′-CCTCTATGCCAACACAGTGC-3′;
Nfatc1 Forward: 5′-CGGTAACACCACCCAGTATACC-3′;
Nfatc1 Reverse: 5′-GACTTGATAGGGACCCCATCAC-3′;
Ctsk Forward: 5′-GAAGAAGACTCACCAGAAGCAG-3′;
Ctsk Reverse: 5′-TCCAGGTTATGGGCAGAGATT-3′;
Mmp9 Forward: 5′-TCACTTTCCCTTCACCTTCGAG-3′;
Mmp9 Reverse: 5′-TTGCCGTCCTTATCGTAGTCAG-3′;
Acp5 Forward: 5′-CACTCCCACCCTGAGATTTGT-3′;
Acp5 Reverse: 5′-CATCGTCTGCACGGTTCTG-3′;
PTP4A2 Forward: 5′-CTCTTATGAGAACATGCGTTTTCTG-3′;
PTP4A2 Reverse: 5′-CCGTACTTCTTAAGTTCCTCTGTGAA-3′;
β-ACTIN Forward: 5′-CATGTACGTTGCTATCCAGGC-3′;
β-ACTIN Reverse: 5′-CTCCTTAATGTCACGCACGAT-3′.

Bone resorption assay

BMMs were seeded into hydroxyapatite-coated Osteo Assay Surface 24-well plates (Corning, USA) at a density of 5×10^5 cells and stimulated with 50 ng/mL M-CSF and 100 ng/mL RANKL for 4 days. To assess the resorptive function, adherent cells were removed with 5% sodium hypochlorite solution for 10 min and the wells were washed with deionized water. Bone resorption area was visualized under the microscope and determined with the ImageJ software (NIH, USA) after drying of the plates.

Cell proliferation and apoptosis assay

Cell proliferation was quantified using Cell Counting Kit-8 (CCK-8, YEASEN, China) according to the manufacturer's instructions. Briefly, BMMs or RAW 264.7 cells were seeded into 96-well plates and incubated with 10 μL per well of the reagent for 1 h at 37 °C and proliferation was quantified by measuring the absorbance at 450 nm using a microplate reader. Apoptosis was analyzed after treatment with or without RANKL for 2 days on BMMs or RAW 264.7 cells using the Annexin V-FITC Apoptosis Detection Kit (Invitrogen, USA). Flow cytometric data were acquired on a BD FACSCanto™ II flow cytometer (BD Biosciences, USA) and analyzed using FlowJo software.

Detection of ROS

To measure ROS production after RANKL stimulation, a mixture of 100 ng/mL RANKL, 20 μM luminol (Sigma-Aldrich, USA) and 20 U/mL horseradish peroxidase (HRP, Sigma-Aldrich, USA) was prewarmed at 37 °C. 1×10^5 BMMs or RAW 264.7 cells were resuspended with 100 μL Hank's Balanced Salt Solution (HBSS, Sigma-Aldrich, USA), and then an equal volume of the prewarmed mixture was added. Relative light unit (RLU) was monitored every 30 s for 30 min with a luminometer Gen5 (Biotek, USA).

ROS production was also detected by using the fluorogenic probe 2′, 7′-dichlorofluorescein diacetate (DCF-DA, Sigma-Aldrich, USA). BMMs or RAW 264.7 cells stimulated with or without RANKL for 30 min were incubated with DCF-DA for 30 min at 37 °C in 5% CO_2 and mean fluorescence intensity (MFI) of cells were acquired on a BD FACSCanto™ II flow cytometer (BD Biosciences, USA) and analyzed using FlowJo software.

Western blot

Whole-cell lysates were prepared by suspending cells in RIPA lysis buffer (Beyotime Biotechnology, China), supplemented with 0.1 mM PMSF, for 15 min on ice. The lysates were collected, centrifugated, and quantified using a BCA assay (Sangon Biotech, China) for further experiments. Equal quantities of proteins were separated by SDS-PAGE, transferred to a nitrocellulose membrane, and detected using specific antibodies. The membrane was developed using SuperSignal Western Blot Enhancer (Thermo Fisher Scientific, USA) and detected by Image Quant LAS 4000 mini (GE healthcare, USA). The antibodies used were as follows: mouse anti-PRL2 antibody (Millipore, USA), mouse anti-Rac1-GTP antibody (NewEast Biosciences, USA), rabbit anti-Phospho-SAPK/JNK MAPK (Thr183/Tyr185) antibody, rabbit anti-Phospho-P38 MAPK (Thr180/Tyr182) antibody, rabbit anti-Phospho-P44/42 MAPK (ERK1/2) (Thr202/Tyr204) antibody, rabbit anti-Phospho-IκBα (Ser32) antibody (Cell Signaling Technology, USA), mouse anti-NFATc1 antibody, mouse anti-HA antibody, mouse anti-Myc antibody (Santa Cruz Biotechnology, USA), rabbit anti-LC3B antibody, mouse anti-β-actin antibody (Sigma-Aldrich, USA), mouse anti-Vps4a antibody (Santa Cruz Biotechnology, USA), rabbit anti-LAMP2A antibody (Abcam, USA), HRP-conjugated mouse anti-HA antibody (Santa Cruz Biotechnology, USA), HRP-conjugated mouse anti-Myc antibody (Medical & Biological Laboratories, Japan), HRP-conjugated anti-mouse-IgM antibody (Sangon Biotech, China), HRP-conjugated anti-mouse-IgG antibody, and HRP-conjugated anti-rabbit-IgG antibody (Cell Signaling Technology, USA). Original western blots for the results are supplied as Supplementary Materials.

Protein preparation and GST-pulldown

PRL2-pET302/NT-His, PRL2-C46S/C101S-pET302/NT-His and HSC70-pGEX-4T-1 plasmids were transformed into *E. coli* BL21 cells for protein expression, respectively. Protein expression was initiated by IPTG treatment and bacteria were harvested after 4 h culture, followed by lysis and sonication. The His-tagged PRL2 protein was purified by Ni-NTA Superflow Cartridges (QIAGEN, Germany) and the GST-tagged HSC70 protein was purified on Glutathione Sepharose 4B (GE healthcare, USA) according to the manufacturer's instructions.

For the preparation of oxidized and reduced PRL2, the His-tagged PRL2 protein was incubated with 5 mM H_2O_2 to be oxidized His-tagged PRL2 for 30 min at room temperature. The reactions were stopped by adding 12.5 U of catalase (Sigma-Aldrich, USA) to consume H_2O_2. Reduced His-tagged PRL2 was further incubated with 20 mM DTT for 20 min at room temperature.

GST pulldown was performed using GST and GST-HSC70 Sepharose beads. 200 μg His-tagged PRL2 protein was incubated with 20 μL GST and GST-HSC70 Sepharose beads in a total volume of 200 μL of binding buffer (20 mM HEPES supplemented with 0.1% Triton-X 100) for 2 h at 4 °C with rotation. After washing the beads twice with wash buffer (15 mM HEPES, and 250 mM NaCl), the beads were added to non-reducing sample buffer (0.25 M Tris, pH6.8, supplemented with 10% SDS, 0.5% bromophenol blue, and 50% glycerol) and the samples were separated on a 10% SDS-PAGE, followed by Coomassie Blue R-250 staining.

Co-Immunoprecipitation (Co-IP)

HEK293T cells overexpressing Myc-tagged PRL2 and HA-tagged HSC70 were lysed in 200 μL CelLytic™ M (Sigma-Aldrich, USA) supplemented with 0.1 mM PMSF and 1× Protease Inhibitor Cocktail (Roche, Germany). The extracts were assayed for protein content after clarification by high-speed centrifugation at 4 °C. Co-IP was performed using Dynabeads™ Protein G (Invitrogen, USA). In brief, 0.45 mg beads were coated with 1.5 μg specific antibodies for 1 h at 4 °C with rotation. After removing unbound antibody, the bead-antibody complex was incubated with cell lysate for 4 h at 4 °C with rotation. The captured Dynabeads/Ab/Ag complex was washed twice with PBS and boiled in 2× sample buffer. The eluted proteins were separated by SDS-PAGE and detected by Western blot.

Immunofluorescence

HEK293T or RAW 264.7 cells were seeded on round coverslips in 24-well plates for immunofluorescence. After transfection for 24 h, cells were washed twice with prewarmed PBS, fixed with 4% PFA in PBS for 15 min at 37 °C, followed by washing with prewarmed PBS, permeabilization with 0.1% saponin/3% BSA for 15 min, washed again, and blocking using 3% BSA for 45 min. The cells were then stained with primary antibodies at 4 °C overnight, followed by incubation with fluorochrome conjugated secondary antibodies at room temperature for 1 h in the dark. The slides were washed and then mounted using ProLong™ Gold Antifade Mountant with DAPI (Thermo Fisher Scientific, USA). Fluorescence was captured by a laser confocal microscope Leica TCS SP8 (Leica, Germany) at 63X magnification. The antibodies used were as follows: mouse anti-HA antibody (Sigma-Aldrich, USA), rabbit anti-LAMP1 antibody (Abcam, USA), rabbit anti-LAMP2A antibody (Abcam, USA), mouse anti-Myc Alexa Fluor 647 conjugate antibody, goat anti-mouse IgG Alexa Fluor 488 conjugate antibody, and goat anti-rabbit IgG Alexa Fluor 594 conjugate antibody (Cell Signaling Technology, USA).

Pearson's correlation coefficient was used to quantify the degree of colocalization, with 15-20 images/group.

Detection of CMA activity

CMA activity can be performed by the pLVX-KFERQ-PA-mCherryN1 plasmid transfection in cells according to the protocol [18]. The plasmid was kindly

provided from Qian Zhao's lab from Shanghai Jiao Tong University School of Medicine. In brief, RAW 264.7 cells were transfected with the plasmid. For CMA activity analysis, cells were photoactivated by a 405/20-nm LED array, followed by treatment, and were then fixed and co-stained with DAPI. The Z-stack confocal images were acquired using a laser confocal microscope Leica TCS SP8 at 63X magnification. Activation of CMA activity was calculated as the number of fluorescence puncta per cell and quantification analysis was performed with LASAF 3D Viewer (Leica, Germany). The usage of lysosomal protease inhibitors was described previously [38].

LPS-induced inflammatory osteolysis

A mouse skull osteolysis model was used to investigate local osteolysis in vivo. 6-week-old WT and CKO mice were injected subcutaneously with LPS (5 mg/kg/d) over the sagittal midline suture of the calvaria under mild anesthesia for 7 days. At the end of the experiment the mice were killed and the calvaria were excised, fixed in 4% PFA, decalcified with EDTA, embedded in paraffin, and processed for TRAP staining.

K/B×N serum transfer-induced arthritis

K/B×N mice that spontaneously develop arthritis were generated by crossing K/B mice with NOD/Lt mice as described previously [39, 40]. Serum samples were collected from 8-week-old arthritic K/B×N mice. The serum samples were pooled and stored at −80 °C until use. Arthritis was induced by intraperitoneal injection of 200 µL K/B×N serum at day 0 and day 2 in 6-week-old C57BL/6 mice, and the development of arthritis was monitored as described previously [41]. HCQ (SPH Zhongxi Pharmaceutical Co., Ltd., China) was administrated by oral gavage at a dose of 80 mg/kg/d of HCQ from day 0 to day 15 and the mice were then sacrificed. In the control group, mice received an equal volume of saline instead.

Preparation of anti-PRL2 polyclonal antibody and conjugation of proteins to FITC

PRL2 antiserum was prepared in C57BL/6 mice. Recombinant PRL2 protein was formulated with either Freund's complete (primary) or Freund's incomplete (two boosts at two weekly intervals) adjuvant (Sigma-Aldrich, USA) and injected subcutaneously into the animals. Animals were sacrificed 2 weeks after the final antigen immunization. Immunoglobulins from sera were first precipitated with ammonium sulfate and then purified using Protein A/G PLUS-Agarose Beads (Santa Cruz Biotechnology, USA) according to the manufacturer's instructions. The purified mouse anti-PRL2 antibodies were conjugated to FITC using the FluoroTag™ FITC Conjugation Kit (Sigma-Aldrich, USA) according to the manufacturer's instructions.

Flow cytometry

For surface staining, cells were washed once in FACS buffer (0.5% BSA in PBS), blocked with normal mouse serum for 10 min at 4 °C, incubated with antibodies for 30 min at 4 °C, followed by washing with FACS buffer and fixation using 0.5% PFA in FACS buffer. For intracellular staining cells were fixed and permeabilized with BD Fixation/Permeabilization solution (BD Biosciences, USA) for 10 min at 4 °C, followed by washing with BD Perm/Wash™ buffer. Cells were then incubated with mouse anti-PRL2 FITC conjugated antibody for 30 min at 4 °C, followed by washing with BD Perm/Wash™ buffer. Flow cytometric data were acquired on a BD FACSCanto™ II flow cytometer and analyzed using FlowJo software. Antibodies were as follows: rat anti-mouse CD3e APC antibody, rat anti-mouse B220 PE-Cyanine7 antibody, rat anti-mouse CD11b PE antibody, rat anti-mouse Ly-6C APC antibody, rat anti-mouse Ly-6G PE-Cyanine7 antibody, mouse anti-human CD3 PerCP-Cyanine5.5 antibody, mouse anti-human CD14 PE antibody, and mouse anti-human CD19 APC antibody (Invitrogen, USA).

Statistical analyses

The data were presented as mean ± s.e.m. from two or more independent experiments. Statistical analyses were performed using GraphPad Prism 8 software. Statistical significance was calculated using the unpaired, two-tailed Student's *t*-test or one-way ANOVA followed by post hoc Tukey's test as detailed in the figure legends. $P < 0.05$ were considered to indicate a significant difference. Asterisks used to indicate significance correspond to the following: $^{*}P < 0.05$, $^{**}P < 0.01$, $^{***}P < 0.005$.

DATA AVAILABILITY

All data needed to evaluate the conclusions in the paper are present in the paper and/or the Supplementary Materials. Additional data related to this paper may be requested from the authors.

REFERENCES

1. Takayanagi H. Inflammatory bone destruction and osteoimmunology. J Periodont Res. 2005;40:287–93.
2. Gibon E, Lu LY, Nathan K, Goodman SB. Inflammation, ageing, and bone regeneration. J Orthop Transl. 2017;10:28–35.
3. Mbalaviele G, Novack DV, Schett G, Teitelbaum SL. Inflammatory osteolysis: a conspiracy against bone. J Clin Invest. 2017;127:2030–9.
4. Dubrovsky AM, Lim MJ, Lane NE. Osteoporosis in rheumatic diseases: anti-rheumatic drugs and the skeleton. Calcif Tissue Int. 2018;102:607–18.
5. Park JH, Lee NK, Lee SY. Current understanding of RANK signaling in osteoclast differentiation and maturation. Mol Cells. 2017;40:706–13.
6. Kim JH, Kim N. Signaling pathways in osteoclast differentiation. Chonnam Med J. 2016;52:12–17.
7. Ono T, Nakashima T. Recent advances in osteoclast biology. Histochem Cell Biol. 2018;149:325–41.
8. Gambari L, Grassi F, Roseti L, Grigolo B, Desando G. Learning from monocyte-macrophage fusion and multinucleation: potential therapeutic targets for osteoporosis and rheumatoid arthritis. Int J Mol Sci. 2020;21:6001.
9. Tsukasaki M, Takayanagi H. Osteoimmunology: evolving concepts in bone-immune interactions in health and disease. Nat Rev Immunol. 2019;19:626–42.
10. Lee NK, Choi YG, Baik JY, Han SY, Jeong DW, Bae YS, et al. A crucial role for reactive oxygen species in RANKL-induced osteoclast differentiation. Blood. 2005;106:852–9.
11. Agidigbi TS, Kim C. Reactive oxygen species in osteoclast differentiation and possible pharmaceutical targets of ROS-mediated osteoclast diseases. Int J Mol Sci. 2019;20:3576.
12. Teitelbaum SL, Ross FP. Genetic regulation of osteoclast development and function. Nat Rev Genet. 2003;4:638–49.
13. Shalev M, Elson A. The roles of protein tyrosine phosphatases in bone-resorbing osteoclasts. Biochim Biophys Acta-Mol Cell Res. 2019;1866:114–23.
14. Yin C, Wu C, Du X, Fang Y, Pu J, Wu J, et al. PRL2 controls phagocyte bactericidal activity by sensing and regulating ROS. Front Immunol. 2018;9:2609.
15. Du X, Zhang Y, Li X, Li Q, Wu C, Chen G, et al. PRL2 serves as a negative regulator in cell adaptation to oxidative stress. Cell Biosci. 2019;9:96.
16. Yim WW-Y, Mizushima N. Lysosome biology in autophagy. Cell Disco. 2020;6:6.
17. Tekirdag K, Cuervo AM. Chaperone-mediated autophagy and endosomal microautophagy: Jointed by a chaperone. J Biol Chem. 2018;293:5414–24.
18. Juste YR, Cuervo AM. Analysis of chaperone-mediated autophagy. Methods Mol Biol. 2019;1880:703–27.
19. Zeng Q, Si X, Horstmann H, Xu Y, Hong W, Pallen CJ. Prenylation-dependent association of protein-tyrosine phosphatases PRL-1, -2, and -3 with the plasma membrane and the early endosome. J Biol Chem. 2000;275:21444–52.
20. Koga H, Martinez-Vicente M, Macian F, Verkhusha VV, Cuervo AM. A photoconvertible fluorescent reporter to track chaperone-mediated autophagy. Nat Commun. 2011;2:386.
21. Kaushik S, Cuervo AM. The coming of age of chaperone-mediated autophagy. Nat Rev Mol Cell Biol. 2018;19:365–81.
22. Kirchner P, Bourdenx M, Madrigal-Matute J, Tiano S, Diaz A, Bartholdy BA, et al. Proteome-wide analysis of chaperone-mediated autophagy targeting motifs. PLoS Biol. 2019;17:e3000301.
23. Schrezenmeier E, Dörner T. Mechanisms of action of hydroxychloroquine and chloroquine: implications for rheumatology. Nat Rev Rheumatol. 2020;16:155–66.
24. Coury F, Peyruchaud O, Machuca-Gayet I. Osteoimmunology of bone loss in inflammatory rheumatic diseases. Front Immunol. 2019;10:679.
25. Briot K, Geusens P, Em Bultink I, Lems WF, Roux C. Inflammatory diseases and bone fragility. Osteoporos Int. 2017;28:3301–14.
26. Kichaev G, Bhatia G, Loh P-R, Gazal S, Burch K, Freund MK, et al. Leveraging polygenic functional enrichment to improve GWAS power. Am J Hum Genet. 2019;104:65–75.
27. Sakaue S, Kanai M, Tanigawa Y, Karjalainen J, Kurki M, Koshiba S, et al. A cross-population atlas of genetic associations for 220 human phenotypes. Nat Genet. 2021;53:1415–24.
28. Cuervo AM. Chaperone-mediated autophagy: selectivity pays off. Trends Endocrinol Metab. 2010;21:142–50.
29. Funato Y, Miki H. Reversible oxidation of PRL family protein-tyrosine phosphatases. Methods. 2014;65:184–9.
30. Rubio T, Kohn M. Regulatory mechanisms of phosphatase of regenerating liver (PRL)-3. Biochem Soc Trans. 2016;44:1305–12.

31. Wei M, Korotkov KV, Blackburn JS. Targeting phosphatases of regenerating liver (PRLs) in cancer. Pharm Ther. 2018;190:128–38.
32. Kiffin R, Christian C, Knecht E, Cuervo AM. Activation of chaperone-mediated autophagy during oxidative stress. Mol Biol Cell. 2004;15:4829–40.
33. Aletaha D, Neogi T, Silman AJ, Funovits J, Felson DT, Bingham CO 3rd, et al. 2010 rheumatoid arthritis classification criteria: an American College of Rheumatology/European League against Rheumatism collaborative initiative. Ann Rheum Dis. 2010;69:1580–8.
34. Zhou YM, Yang YY, Jing YX, Yuan TJ, Sun LH, Tao B, et al. BMP9 reduces bone loss in ovariectomized mice by dual regulation of bone remodeling. J Bone Min Res. 2020;35:978–93.
35. Stegen S, Stockmans I, Moermans K, Thienpont B, Maxwell PH, Carmeliet P, et al. Osteocytic oxygen sensing controls bone mass through epigenetic regulation of sclerostin. Nat Commun. 2018;9:2557.
36. Kuma A, Hatano M, Matsui M, Yamamoto A, Nakaya H, Yoshimori T, et al. The role of autophagy during the early neonatal starvation period. Nature. 2004;432:1032–6.
37. Wang Z, Fayngerts S, Wang P, Sun H, Johnson DS, Ruan Q, et al. TIPE2 protein serves as a negative regulator of phagocytosis and oxidative burst during infection. Proc Natl Acad Sci USA. 2012;109:15413–8.
38. Dong S, Wang Q, Kao YR, Diaz A, Tasset I, Kaushik S, et al. Chaperone-mediated autophagy sustains haematopoietic stem-cell function. Nature. 2021;591:117–23.
39. Kouskoff V, Korganow AS, Duchatelle V, Degott C, Benoist C, Mathis D. Organ-specific disease provoked by systemic autoimmunity. Cell. 1996;87:811–22.
40. Monach PA, Mathis D, Benoist C. The K/BxN arthritis model. Curr Protoc Immunol. 2008;81:15.22.11–15.22.12.
41. Murata K, Fang C, Terao C, Giannopoulou EG, Lee YJ, Lee MJ, et al. Hypoxia-sensitive COMMD1 integrates signaling and cellular metabolism in human macrophages and suppresses osteoclastogenesis. Immunity. 2017;47:66–79.

ACKNOWLEDGEMENTS

We are grateful to Dr. Qing Zhong for providing reagents including Torin1 (Selleck Chemicals, USA), and rabbit anti-LC3B antibody. We thank Dr. Qian Zhao for providing the pLVX-KFERQ-PA-mCherryN1 plasmid. We would like to thank Dr. Fubin Li for providing K/B mice. We would like to thank Dr. Huabing Li for providing RAW 264.7 cells expressing Cas9. Last, we would like to thank Dr. Helena Helmby for editing the manuscript.

AUTHOR CONTRIBUTIONS

ZW generated the initial ideas and proposed the hypotheses. ZW, QL, XD, ZT, and JL designed the study. ZW and GC supervised the study. QL and XD conducted the key experiments. BR, SK, CL, JC, CW, and XN performed experiments. TY, WW, and WX provided the human samples. KL and BL provided reagents. XD provided the animals. ZW, QL, and ZT performed the data analysis, interpretation of the results and wrote the manuscript.

FUNDING

This work was supported by the National Natural Science Foundation of China (81971486), the Natural Science Foundation of Shanghai (19ZR1428500), and Innovative research team of high-level local universities in Shanghai, the Fifth Round of Three-Year Public Health Action Plan of Shanghai (No. GWV-10.1-XK13).

COMPETING INTERESTS

The authors declare no competing interests.

ETHIC APPROVAL

Human subject research was approved by the Ethics Committee of Guanghua Hospital Affiliated to Shanghai University of Traditional Chinese Medicine (Project number 2021-K-46), and all subjects provided signed informed consent. This study has been registered at chictr.org.cn (ChiCTR2100046850). All animal experiments were approved by the Institutional Animal Care and Use Committee (IACUC) of Shanghai Jiao Tong University School of Medicine (Project number A-2019-053, A-2019-069).

ADDITIONAL INFORMATION

Supplementary information The online version contains supplementary material available at https://doi.org/10.1038/s41418-022-01068-y.

Correspondence and requests for materials should be addressed to Guangjie Chen or Zhaojun Wang.